



Interplanetary energetic electrons observed in Earth's polar cusp/cap/lobes

Linghua Wang¹

Received: 15 January 2022 / Accepted: 25 April 2022 / Published online: 25 May 2022
© The Author(s) 2022

Abstract

The Earth's polar cusp, cap and lobes are the important boundaries to transport the plasma and energy from the interplanetary medium to terrestrial magnetosphere. Interplanetary energetic electrons, mainly consisting of continuous solar wind superhalo electrons and transient solar energetic electron events both with typical power-law energy spectra, can provide a source of energetic electrons to the Earth's magnetosphere. After briefly summarizing recent results of solar wind superhalo electrons and solar energetic electron events, this paper reviews the first evidences for the direct and continuous entry of energetic electrons from the interplanetary medium to the Earth's polar cusp, cap and/or lobes, observed by one Chinese Bei-Dou navigation satellite. Such entering electrons can make a possible contribution to the generation of magnetospheric energetic electrons.

Keywords Energetic electrons · Solar wind superhalo electrons · Solar energetic electrons · Interplanetary medium · Magnetosphere · Polar cusp

1 Introduction

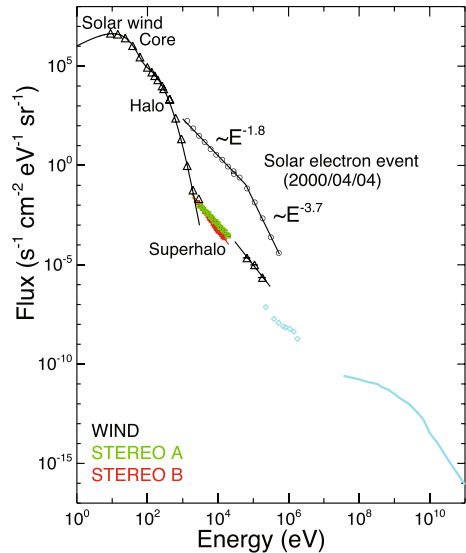
The Earth's polar cusp, cap and lobes are the important boundaries to transport the plasma and energy from the interplanetary medium (IPM) to terrestrial magnetosphere (Zong et al. 2005). Using the Polar, Cluster and MMS measurements (Escoubet et al. 2001; Burch et al. 2016), many studies showed that some > 40 keV electrons occasionally occur in the external cusp regions (e.g., Sheldon et al. 1998; Zhang et al. 2005; Asikainen and Mursula 2006; Walsh et al. 2010; Nykyri et al. 2012, 2019). These studies proposed that those energetic electrons probably originate from the magnetosphere or a local acceleration process.

Interplanetary energetic electrons (Fig. 1), mainly consisting of solar wind superhalo electrons and solar energetic electron (SEE) events, can be another energetic

✉ Linghua Wang
wanglhwang@gmail.com; wanglhwang@pku.edu.cn

¹ School of Earth and Space Sciences, Peking University, Beijing 100871, China

Fig. 1 Interplanetary electron flux versus energy spectrum from ~ 10 eV to 1 TeV at 1 AU. The black triangles, colored squares and blue diamonds denote the solar wind electron populations observed at quiet times by Wind, STEREO and IMP-7 (Hurford 1974; Wang et al. 2012a), and the blue curve shows the galactic cosmic-ray electrons detected by IMP-6 (Lin 1974). The black circles represent a SEE event observed by Wind on April 04, 2000 (Krucker et al. 2009). Figure is taken from Cohen et al. (2021)



electron source for the terrestrial polar cusp, cap and lobes. In the solar wind, superhalo electrons are continuously present at energies above ~ 2 keV, even unaccompanied by significant interplanetary and/or solar activities (Wang et al. 2012a). At quiet times, superhalo electrons typically exhibit a roughly isotropic pitch angle distribution and a single-power-law energy spectrum with an average power-law index of ~ 2.4 at energies of ~ 2 –200 keV (Wang et al. 2012a, 2015; Yang et al. 2015a). SEE events (Lin 1985; Wang et al. 2012b; Cohen et al. 2021), typically observed at energies of ~ 1 –100s keV, are thought to be caused by the particle acceleration processes associated with solar eruptions, e.g., solar flares and/or coronal mass ejections (CMEs). SEEs often beam antisunwards along the interplanetary magnetic field (IMF) and show a double-power-law energy spectrum that steepens at energies above ~ 60 keV (Cohen et al. 2021, and references therein).

In this paper, we briefly summarize recent results of solar wind superhalo electrons and SEE events measured by the Wind and STEREO spacecraft in the IPM (Sect. 2). Then we review the observational evidences that these interplanetary electrons enter the terrestrial polar cusp, cap and/or lobes (Sect. 3), by combining the electron measurements from the Wind spacecraft at the Lagrange 1 (L1) point and from one Chinese BeiDou navigation satellite in an inclined geosynchronous orbit (IGSO).

2 Interplanetary energetic electrons

In situ electron measurements at 1 AU show that interplanetary energetic electrons at energies from ~ 2 to 100s keV mostly comprise continuous solar wind superhalo electrons, occasionally superimposed by some transient SEE events (Fig. 1). In this section, we briefly review recent observations of superhalo electrons and SEE

events, made in situ by the three-dimensional Plasma and Energetic Particle instrument (3DP) onboard the Wind spacecraft and/or by the SupraThermal Electron instrument (STE) onboard the STEREO spacecraft (Lin et al. 1995; Lin 2008).

Since its launch in November 1994, the Wind spacecraft was first placed in highly elliptical earth orbits, and then remains in halo orbits around the L1 point after mid-May 2004 (Wang 2009). The onboard 3DP instrument provides the full three-dimensional electron (ion) distributions at energies from the solar wind thermal plasma to ~ 400 keV (~ 6 MeV) with a pitch-angle resolution of 22.5° (Lin et al. 1995; Wang 2009). In the 3DP instrument, electron electrostatic analyzers detect the electrons at energies up to 30 keV with a channel energy resolution of $\Delta E/E \approx 0.2$, while silicon semiconductor telescopes (SST) observe the ~ 25 – 400 keV electrons in the foil (F) detectors and the ~ 20 keV– 6 MeV ions in the open (O) detectors, with a channel energy resolution of $\Delta E/E \approx 0.3$. In the SST, the F detectors utilize a thin Lexan foil to reject protons up to 400 keV but hardly affect the $\gtrsim 25$ keV electrons.

After the launch in October 2006, the STEREO A (B) spacecraft was put in a nominal heliocentric orbit ahead (behind) the Earth, leaving the Earth at a longitude rate of $\sim 22^\circ$ per year. In the onboard IMPACT investigation (Luhmann 2008), the STE instrument (Lin 2008) uses thin-window silicon semiconductor detectors, coupled with the state-of-the-art pulse-reset front-end electronics, to measure electrons at energies of ~ 2 – 100 keV with an energy resolution of $\lesssim 1$ keV FWHM. It consists of two oppositely directed sets (STE-U and STE-D) of four detectors, respectively, to detect electrons coming in the antisunward and sunward directions. Unfortunately, STE-U mounted on the front of spacecraft is saturated by multiply scattered sunlight at the spacecraft surface, in the nominal attitude. STE-D has a total FWHM field of view (FOV) of 67° ecliptic longitude \times 65° (-32.5° to 32.5°) latitude centered on the nominal direction of Parker's spiral IMF, each detector (D0, D1, D2 and D3) with a FOV of 16.8° longitude \times 65° latitude.

2.1 Solar wind superhalo electrons

At quiet times (Fig. 1), interplanetary electrons are dominated by the solar wind electron populations: a thermal Maxwellian core with a temperature ~ 10 eV (e.g., Montgomery et al. 1968; Rosenbauer et al. 1977; Pilipp 1987), a suprathermal halo/strahl with a Kappa-distribution spectrum (e.g., Maksimovic et al. 1997; Štverák et al. 2009; Tao et al. 2021), and a $\gtrsim 2$ keV superhalo with a power-law spectrum (e.g., Wang et al. 2012a, 2015). Specifically, Wang et al. (2012a, 2015) defined a quiet time period as a >12 -hour time period when the suprathermal electron measurements exhibit no significant temporal variations at energies above ~ 2 keV (Figs. 2 and 3). Due to the instrumental sensitivity, the quiet-time superhalo electrons can be efficiently detected by STEREO/STE at ~ 2 – 20 keV and by Wind/3DP at ~ 25 – 200 keV. Figure 2 shows one example of solar wind superhalo electrons observed by STE-D onboard STEREO B at quiet times on November 28–29, 2007. The observed velocity distribution functions (VDFs) appear to be independent of detector looking directions (also see Figure 4a) and of the varying IMF. These

Fig. 2 Quiet-time observations of solar wind superhalo electrons by STEREO B. Top panel: the superhalo electron VDFs detected by STE-D1 (pink) and STE-D3 (green) at 3.1, 7.0 and 19 keV (center channel energy). The two vertical dashed lines denote a 2-hour quiet-time sample selected on November 29, 2007. Bottom panels: the IMF magnitude, polar angle and azimuthal angle. Figure is taken from Wang et al. (2012a)

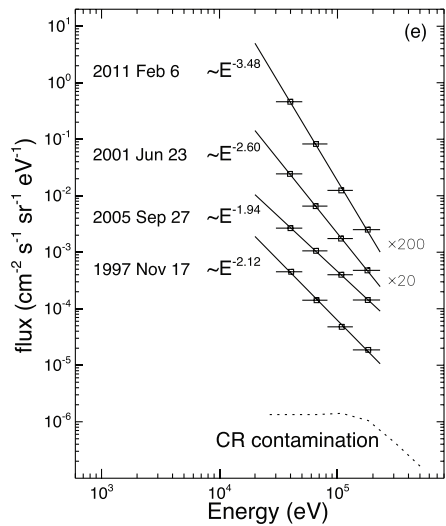
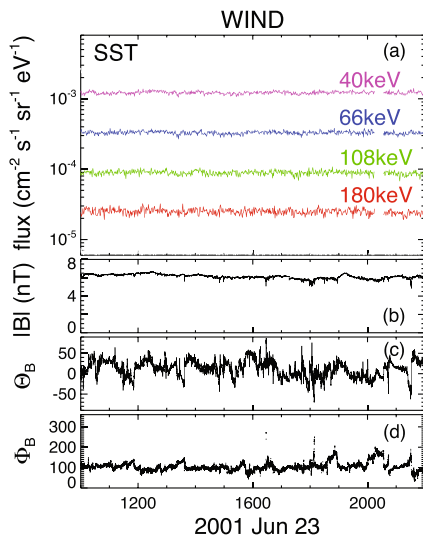
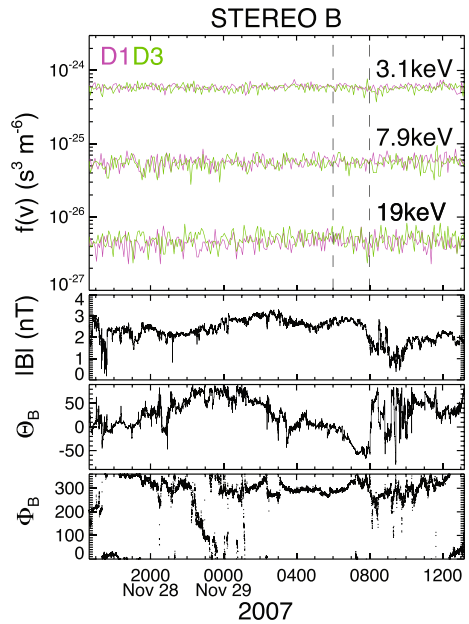


Fig. 3 Quiet-time observations of solar wind superhalo electrons by Wind. **a** A 12-hour quiet-time sample of superhalo electron omnidirectional differential fluxes detected by Wind/3DP at 40, 66, 108 and 180 keV (center channel energy) on June 23, 2001. (b-d): the IMF magnitude, polar angle and azimuthal angle. **b** The average superhalo electron flux energy spectrum at ~25–200 keV for four quiet-time samples, after removal of contaminations due to galactic cosmic rays. The power-law spectrum fit is denoted by the solid straight lines. Figure is taken from Wang et al. (2015)

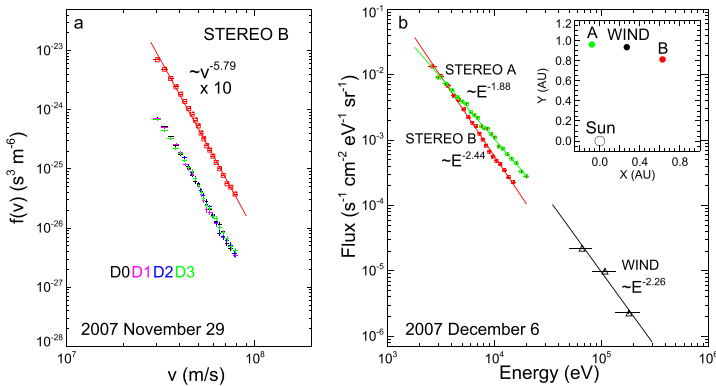


Fig. 4 Quiet-time superhalo electron energy spectra after removal of instrumental noise/contamination. **a** The average superhalo electron VDFs measured at $\sim 2\text{--}20$ keV by STE-D(0,1,2, and 3) onboard STEREO B, for the quiet-time sample on November 29, 2007. The red squares represent the superhalo electron VDF averaged over four STE-D detectors, multiplying by a factor of 10. **b** The superhalo electron omnidirectional flux versus energy spectra detected by Wind (black) and STEREO (green and red) on December 6, 2007. The insert plots the average location of Wind and STEREO projected onto the ecliptic plane, for the shown quiet-time samples. Figure is taken from Wang et al. (2012a)

indicate that quiet-time superhalo electrons are essentially isotropic in angular distribution, consistent with the statistical survey by Yang et al. (2015a).

For the STEREO/STE observations of solar wind superhalo electrons at $\sim 2\text{--}20$ keV (Fig. 2) from March 2007 through March 2009, Wang et al. (2012a) identified 235 quiet-time samples by selecting a 2-hour quiet-time interval per day (when available). For the Wind/3DP measurements of superhalo electrons at $\sim 25\text{--}200$ keV (Fig. 3) from January 1995 through December 2013, Wang et al. (2015) identified 242 quiet-time samples by choosing a 12-hour quiet-time interval per day (when available). For these samples of quiet-time superhalo electrons (Figs. 3, 4 and 5), the average background-subtracted electron differential flux fits well to a single-power-law energy function: $J \propto E^{-\gamma}$, where γ is the power-law spectral index. At $\sim 2\text{--}20$ keV ($\sim 25\text{--}200$ keV), the fitted γ varies from ~ 1.3 to ~ 3.3 (from ~ 1.6 to ~ 3.7) with an average value of $\sim 2.25 \pm 0.41$ (2.43 ± 0.37). This indicates that superhalo electrons can have a single-power-law energy spectrum at the entire range of $\sim 2\text{--}200$ keV, with a typical $\gamma \sim 2.4$.

In the IPM, superhalo electrons appear to be continuously present, even unaccompanied by significant interplanetary and/or solar activities (Wang et al. 2012a, 2015). In fact, quite-time superhalo electrons exhibit no clear correlations with the monthly sunspot number (Fig. 6), solar flares, microflares, active regions, CMEs, type III radio bursts, stream interaction regions, solar wind core/halo/strahl populations, etc.

If superhalo electrons originate from the Sun, they could be generated by the particle acceleration process in the source region of solar wind (Lin 1997; Wang et al. 2012a, 2015), e.g., by continual nanoflares/microflares or waves (Parker 1988; Scudder 1992). A numerical simulation study showed that in the solar wind source region, the electric field produced in magnetic reconnection region can accelerate

Fig. 5 Histograms of the power-law spectral index γ observed by STEREO/STE at $\sim 2\text{--}20$ keV from March 2007 through March 2009 (top) and by Wind/3DP at $\sim 25\text{--}200$ keV from 1995 through 2013 (bottom). In bottom panel, the red histogram denotes the quiet-time samples detected near solar maximum, while the black histogram represents all 242 quiet-time samples during the 19 years. Figure is taken from Wang et al. (2012a), Wang et al. (2015)

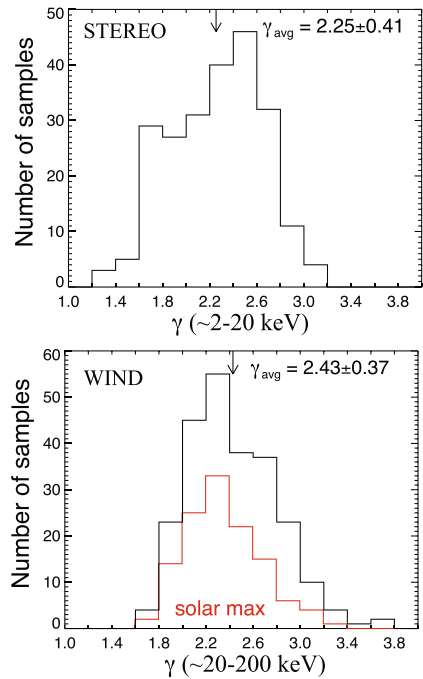
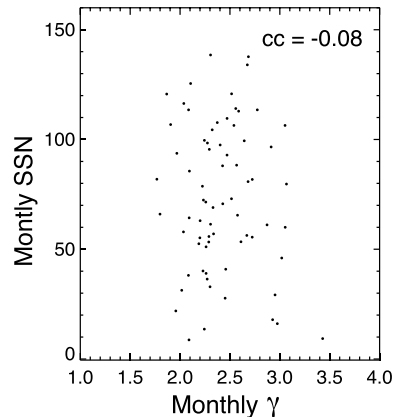


Fig. 6 Scatter plot between the monthly sunspot number and monthly spectral index γ of quiet-time superhalo electrons detected at $\sim 25\text{--}200$ keV by Wind/3DP, from 1995 through 2013. Figure is taken from Wang et al. (2015)



the thermal electrons to energies up to 200 keV, forming a power-law energy spectrum with a $\gamma \sim 1.5\text{--}2.4$ (Yang et al. 2015b). After some accelerated electrons propagate upwards and escape along the open magnetic field into the IPM, they would undergo some unknown scattering process to become nearly isotropic in angular distribution. Another possible scenario is that superhalo electrons could be formed by the the accumulative acceleration processes in the IPM, e.g., shock acceleration at interplanetary shocks (and/or planetary bow shocks), stochastic processes and wave-particle interactions (e.g., Fisk et al. 2010; Yoon et al. 2012; Zank et al. 2014; Yoon

2018; Yang et al. 2019; Liu et al. 2000). The radial dependence of superhalo electron intensity and anisotropy would reflect the nature of source, acceleration and propagation of superhalo electrons. Future investigations would need to combine high-sensitivity measurements from multiple spacecraft such as Solar Orbiter (Müller et al. 2020), Parker Solar Probe (Fox et al. 2016), Wind and STEREO.

2.2 Solar energetic electron events

SEE events are the most frequent solar particle acceleration phenomenon observed in situ by a spacecraft in the IPM (e.g., Lin 1985; Wang et al. 2012b), typically with a narrow antisunward beam along the IMF and a clear energy dispersion at energies of ~ 1 -100s keV (i.e., the slower electrons arrive later at the spacecraft than the faster electrons; see Fig. 7). SEE events are often accompanied by ^3He -rich heavy ions (instead of solar energetic protons), forming a very peculiar solar particle acceleration phenomenon related to solar eruptions (Wang 2009; Wang et al. 2012b), e.g., solar flares and CMEs.

Wang et al. (2012b) made a comprehensive study of the 1191 SEE events detected by Wind/3DP near the Earth from 1995 to 2005 (Fig. 8). Out of these SEE events, about 76% are accompanied by significantly ^3He -rich (i.e., the $^3\text{He}/^4\text{He}$ ratio ≥ 0.01 , strongly enriched with respect to the solar wind value of $\sim 5 \times 10^{-4}$) ion emissions observed by ACE/ULEIS (Mason 1998), so-classified as “ ^3He -rich SEE events”; only $\sim 9\%$ are associated with a strong GOES >10 MeV proton event with the peak proton flux $> 1 \text{ cm}^{-2}\text{s}^{-1}\text{sr}^{-1}$. At 1 AU, ^3He -rich

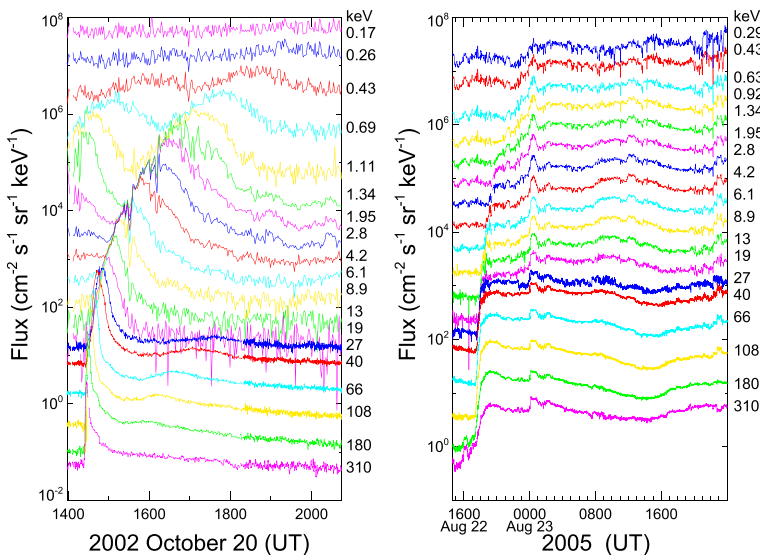
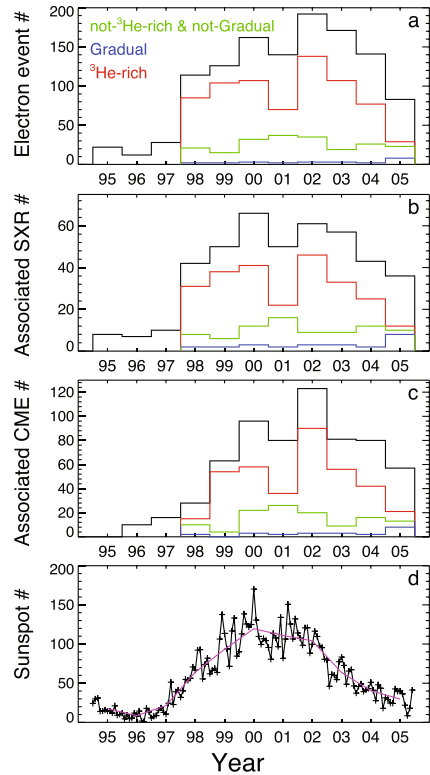


Fig. 7 Comparison of temporal flux profiles between one ^3He -rich SEE event (left) and one gradual SEE event (right) detected by Wind/3DP. The energy labels show the center channel energy. Figure is taken from Wang et al. (2012b)

Fig. 8 Yearly number of SEE events (a), their associated SXR flares/CMEs (b, c) and sunspots (d) from 1995 through 2005. In panels (a–c), the red, blue and green colors denote ^3He -rich, gradual and not- ^3He -rich/not-gradual SEE events, respectively. The black color indicates all the SEE events. In panel d, the pink (black) curve shows the yearly (monthly) sunspot number. Figure is taken from Wang et al. (2012b)

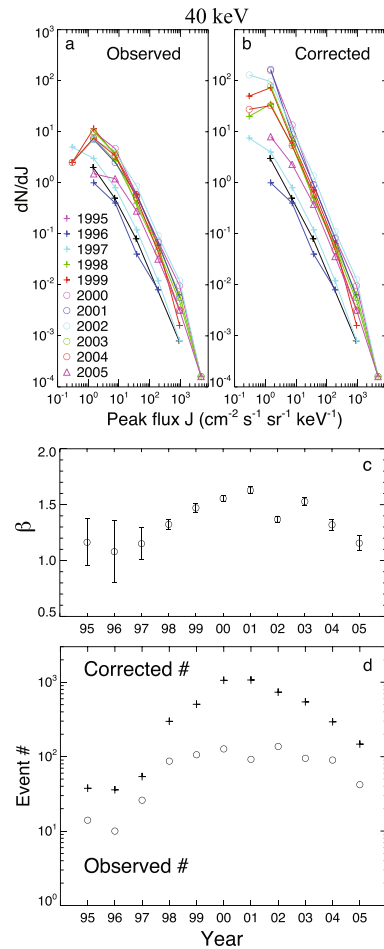


SEE events typically last for from tens of minutes (for a nearly scatter-free propagation in the IPM) to many hours (for a diffusive propagation), extend $\lesssim 45^\circ$ wide in longitude, show an only $\sim 31\%$ association with impulsive (< 1 hour) solar X-ray (SXR) flares, and exhibit a $\sim 60\%$ association with the CMEs taking off the solar west limb.

On the other hand, only $\sim 3\%$ of SEE events are associated with gradual (> 1 hour) SXR flares and not associated with significantly ^3He -rich ion emissions, so-classified as “gradual SEE events” (Fig. 8). At 1 AU, these gradual SEE events generally last for days, extend $\sim 100^\circ$ – 180° in longitude, and show a $\sim 87\%$ association with fast (> 500 km/s) CMEs.

In solar cycle 23 (Fig. 8), the yearly occurrence rate of SEE events observed by Wind/3DP near the Earth varies strongly with the sunspot number (Wang et al. 2012b), from a minimum of 12 in the year 1996 to a double peak of 162 in the year 2000 and 192 in the year 2002 (separated by a dip of 140 in the year 2001) at solar maximum. The yearly occurrence frequency distribution of SEE events can be expressed by plotting dN/dJ as a function of J , where N is the yearly event occurrence rate and J is the event background-subtracted electron peak flux for a given energy channel. At 40 keV (Fig. 9), the observed occurrence frequency distribution can fit to a power-law function of $dN/dJ \propto J^{-\beta}$ with a power-law index β , at large J values; however, it bends downward at small J values, because

Fig. 9 SEE event occurrence frequency at 40 keV near the Earth, from 1995 through 2005. **a–b** the observed and corrected event occurrence differential frequency distributions. N is the yearly event occurrence rate and J is the event electron peak flux after removal of pre-event background. **c** Fitted power-law index β of yearly occurrence frequency distribution. **d** The observed (circles) and corrected (crosses) yearly event occurrence rate. Figure is taken from Wang et al. (2012b)



small SEE events would be unlikely detected if the pre-event background flux is relatively large, e.g., when Wind/3DP is located during the decay phase of some strong events (Fig. 7) or located within the terrestrial bow shock. Wang et al. (2012b) corrected such background effects on the detection of SEE events, by assuming that the event occurrence rate during the high pre-event background period is the same as the observed occurrence rate during the low pre-event background period. At 40 keV, the corrected dN/dJ appears to fit well to the power-law function, when J is above $1 \text{ cm}^{-2} \text{ s}^{-1} \text{ sr}^{-1} \text{ keV}^{-1}$ (that's near the SST's sensitivity). For the eleven years, the fitted β also varies with the solar cycle, from ~ 1.1 at solar minimum to ~ 1.6 at solar maximum.

A corrected yearly occurrence rate of SEE events near the Earth can be obtained by integrating dN over J from the observed minimal peak flux to infinity. At 40 keV (Fig. 9d), it ranges from ~ 35 at solar minimum to ~ 1000 at solar maximum, about ~ 3 -10 times higher than the measured yearly occurrence rate. Therefore, the event

number of SEEs detected near the Earth would likely be greatly underrated since many small events can hardly be detected in the presence of strong pre-event background flux. Furthermore, a total occurrence rate of SEE events over the whole Sun is estimated to be $\sim 10^4 \text{ year}^{-1}$ near solar maximum, since most SEE events show a $\lesssim 45^\circ$ extent in longitude.

For the SEE events observed in situ at 1 AU (Lin et al. 1995; Wang et al. 2006; Krucker et al. 2009; Dresing et al. 2020), the electron peak differential fluxes, J , often fit to a double-power-law energy spectrum that steepens at energies above a break energy E_{br} :

$$J(E) \propto \begin{cases} E^{-\gamma_1}, & E < E_{br} \\ E^{-\gamma_2}, & E > E_{br}. \end{cases} \quad (1)$$

According to a statistical study (Krucker et al. 2009), ^3He -rich SEE events typically show an average spectral index of $\gamma_1 = 1.9 \pm 0.3$ at energies below an average E_{br} near 60 keV and an average index of $\gamma_2 = 3.6 \pm 0.7$ at energies above (Fig. 10).

3 Interplanetary energetic electrons in Earth's polar cusp/cap/lobes

A Chinese BeiDou navigation satellite was put in a 55° inclined IGSO at altitudes of about 42000 km from the Earth's center (Zong et al. 2016), that passes the Earth's high-altitude polar cusp, cap and/or lobes twice per 24-hour orbit. The onboard BeiDa Image Electron Spectrometer (BD-IES) observes the electron (or ion) distributions at energies of 50–600 keV (Zong et al. 2016), with a total FOV of $20^\circ \times 180^\circ$ and a channel energy resolution of $\Delta E/E \approx 0.3$. Unfortunately, this BeiDou satellite

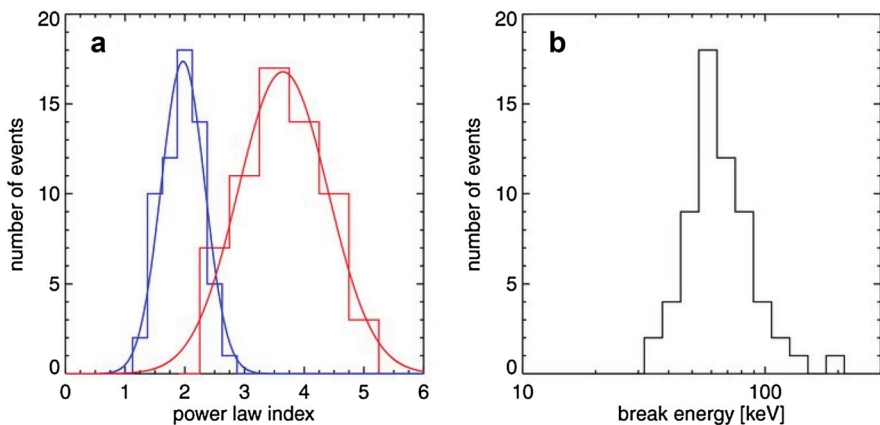


Fig. 10 Histograms of fitted spectral parameters for the 62 ^3He -rich SEE events detected at ~ 1 –300 keV by Wind/3DP in the IPM. **a** Spectral index γ_1 (blue) at energies below the break energy E_{br} and γ_2 (red) at energies above. The blue and red curves show a Gaussian fit. **b** Spectral break energy E_{br} . Figure is taken from Krucker et al. (2009)

does not carry the magnetic field instrument, so the electron pitch angle distribution measurements are not available.

Utilizing the BD-IES measurements from 2015 October to 2016 January, we surveyed energetic electrons occurring in the high-altitude polar cusp, cap and/or lobes (Wang et al. 2017, 2021). Here, we identified the satellite passages of these polar regions by only using the satellite’s location (see Fig. 11, for example), instead of the magnetic field or plasma data, since this IGSO BeiDou satellite has neither magnetic field nor plasma instruments.

We found that when the interplanetary energetic electrons detected by Wind/3DP around the L1 point are made up of solar wind superhalo electrons, the >50 keV measurements by BD-IES in the high-altitude polar cusp, cap and/or lobes are dominated typically by the instrumental noise (due to higher-energy penetrating particles and/or intrinsic background), and very occasionally by some spike-like events with

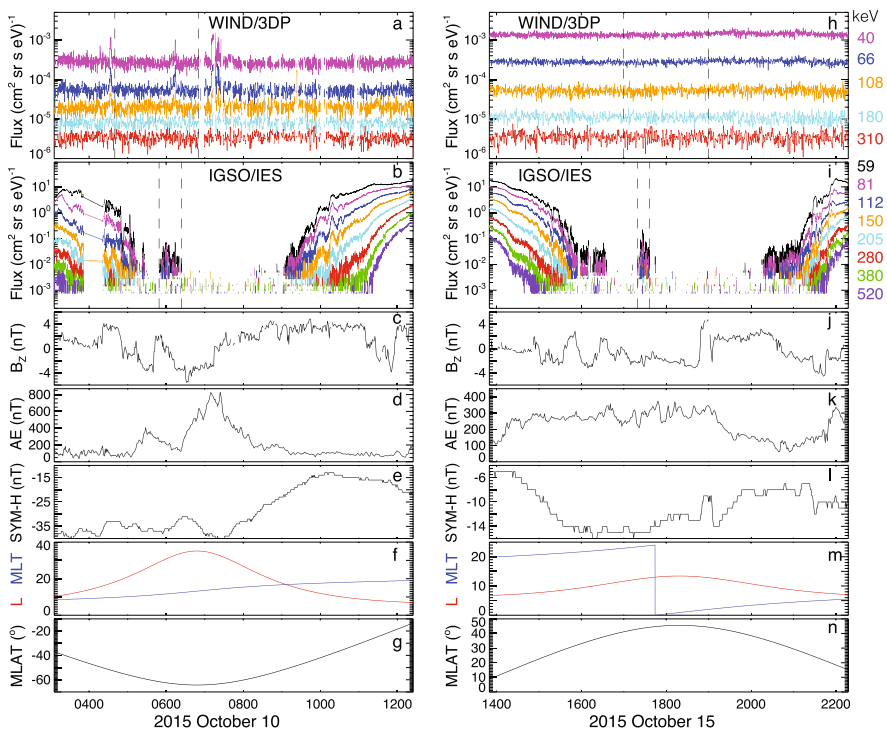


Fig. 11 Temporal profiles of the 2015 October 10 DEE event (left) and 2015 October 15 DEE event (right). **a/h** Electron omnidirectional differential fluxes detected at 40–310 keV by WIND/3DP at the L1 point. **b/i** Electron omnidirectional differential fluxes measured at 59–520 keV by BD-IES in the IGSO orbit. **c/j** The OMNI IMF B_z component in the geocentric solar magnetospheric (GSM) coordinates. **d/k** AE (auroral electrojet) index. **e/l** SYM-H index. **f/m** L shell (red) and MLT (blue) along the IGSO orbit. **g/n** Magnetic latitude along the IGSO orbit. In panels **a** and **h**, the vertical dashed lines denote the selected time interval to obtain the average solar wind superhalo electron energy spectrum. In panels **b** and **i**, the vertical dashed lines denote the selected time interval to obtain the average DEE energy spectrum. Figure is partly taken from Wang et al. (2017)

significant electron fluxes at energies of $\sim 50\text{--}200$ keV, so-called as “discrete energetic electron (DEE) events”. When the interplanetary energetic electrons detected by Wind/3DP are predominated by high-energy SEEs, however, the BD-IES measurements in the polar cusp, cap and/or lobes often show simultaneously strong electron fluxes.

3.1 Solar wind superhalo origin

The IGSO BeiDou satellite makes 103 passages of polar cusp, cap and/or lobes at $L \gtrsim 10$ with the BD-IES measurements available, from 2015 October to 2016 January. During these 103 passages, we identified 28 DEE events that last from ~ 5 minutes to ~ 340 minutes (Wang et al. 2017). Figure 11 plots the overview of two representative DEE events. On October 10, 2015, the interplanetary energetic electrons detected by Wind/3DP are mostly made up of solar wind superhalo electrons, while the IGSO BeiDou satellite passes the southern polar cusp in the dayside during the time interval from $\sim 0530\text{UT}$ to 0900UT (also see Fig. 12). During this southern polar cusp passage, the BD-IES observations are predominated by the instrumental noise at most times; however, they are dominated by a DEE event at $0548\text{--}0624\text{UT}$ when the satellite lies near 1200 magnetic local time (MLT) with an average magnetic latitude of $S47.5^\circ$ and L of ~ 14.5 . On October 15, 2015, the interplanetary energetic electrons detected by Wind/3DP are also made up of solar wind superhalo electrons, while the IGSO BeiDou satellite passes the northern polar cusp/lobe regions in the nightside during the time interval from $\sim 1640\text{UT}$ to 2010UT . During this northern cusp/lobe passage, the BD-IES observations are dominated by a DEE event at $1719\text{--}1736\text{UT}$ when the satellite is near 2330 MLT with an average magnetic latitude of $N43.7^\circ$ and L of ~ 12.6 . Note that the BD-IES observations are predominated by high-flux energetic electrons in outer radiation belts, during the satellite trajectories before and after the cusp/lobe passages.

During the 2015 October 10 DEE event (October 15 DEE event), the $50\text{--}130$ keV ($50\text{--}170$ keV) electrons measured by BD-IES exhibit a power-law energy spectrum of electron differential fluxes as $J \propto E^{-3.2}$ ($E^{-3.6}$), while the $\sim 50\text{--}200$ keV superhalo electrons detected by Wind/3DP in the solar wind also have a power-law spectrum of $J \propto E^{-1.9}$ ($E^{-3.2}$). These DEE spectra appear significantly different from the typical energy spectra of radiation belt electrons that show a double-power-law shape with a downward break near 150 keV (Fig. 13). In addition, the 2015 October 10 event (October 15 event) corresponds to a rather small south component of average OMNI IMF at the Earth’s bow shock nose, an average AE index of ~ 190 nT (~ 280 nT) and an average SYM-H index of ~ 35 nT (~ 15 nT).

Among the 28 DEE events, 22 show good observations of flux versus energy spectrum, with strongly enhanced fluxes over the instrumental noise (i.e. $J > 4J_{\text{noise}}$) in at least three energy channels. These 22 events typically exhibit a single-power-law energy spectrum, $J \propto E^{-\gamma}$, which is analogous to the energy spectrum of superhalo electrons simultaneously detected in solar wind but different from the typical energy spectrum of radiation belt electrons with a downward break near $100\text{--}150$ keV. Figure 14 compares the power-law spectral indexes between the $\sim 50\text{--}200$ keV

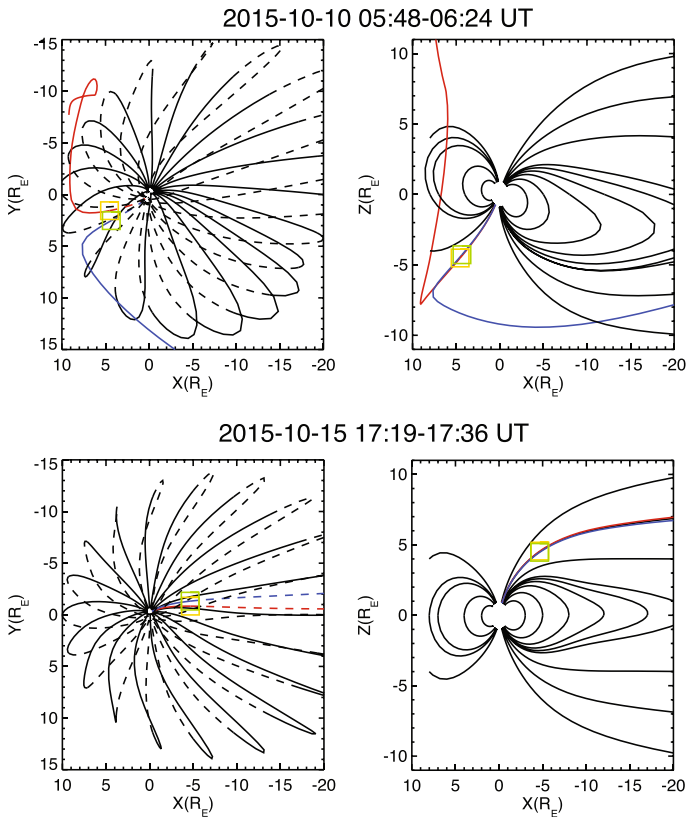


Fig. 12 Average configuration of magnetospheric magnetic field lines (estimated by the T96 model) during the 2015 October 10 DEE event (top) and 2015 October 15 DEE event (bottom), projected onto the X - Y plane and X - Z plane of geocentric solar ecliptic (GSE) coordinates. The BeiDou satellite (shown as square symbols) is connected to the red (blue) magnetic field line at the DEE event's start time (end time). Figure is taken from Wang et al. (2017)

DEEs and ~ 50 – 200 keV simultaneous superhalo electrons (~ 50 – 150 keV radiation belt electrons observed on the same date). For these 22 events, the DEE spectra index γ_{DEE} ranges from 2.6 to 4, mostly larger than the superhalo electron index γ_{SW} and much larger than the radiation belt electron index γ_{RB} . Furthermore, the observed DEE fluxes appear to be weakly correlated with the superhalo electron fluxes detected simultaneously in solar wind. Most of the 28 DEE events also correspond to quiet geomagnetic activities (Fig. 15), i.e., the AE index < 300 nT and the SYM-H index > -20 nT (Zong et al. 2021). These results suggest that the DEE events could arise from the superhalo electrons in solar wind rather than the energetic electrons in radiation belts.

Among the 26 DEE events with the available OMNI IMF data (Fig. 16), 20 events have a south component ($B_z < 0$) of average IMF at the bow shock nose, suggesting that the entry of superhalo electrons from the solar wind to the magnetosphere

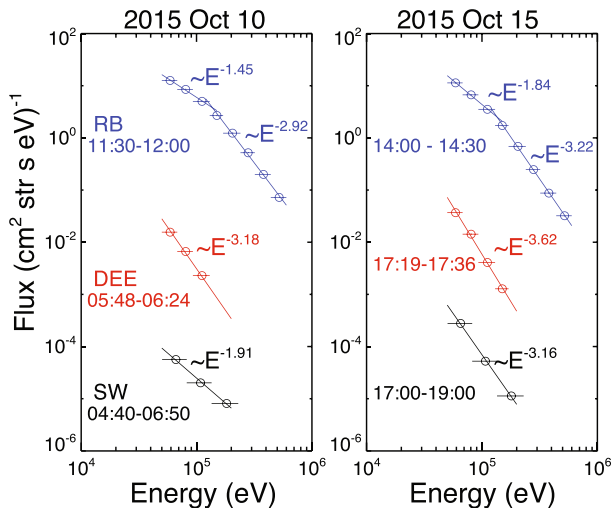


Fig. 13 Comparison of the flux energy spectrum among the DEEs (red), solar wind superhalo electrons (black) and radiation belt electrons (blue), for the 2015 October 10 event (left) and October 15 event (right). Figure is taken from Wang et al. (2017)

can be due to the magnetic reconnection at low-latitude magnetopause; the other 6 events have a north component ($B_z > 0$) of average IMF, indicating that the superhalo entry can be also via the reconnection at mid-latitude/high-latitude magnetopause. In addition, these DEE events exhibit an enhanced flux by a factor of ~ 10 – 1000 and a steeper (softer) energy spectrum, compared to the superhalo electrons measured simultaneously in solar wind. It implies that the DEE formation may involve some further acceleration acting on the entering superhalo electrons.

Among these 28 DEE events (Fig. 16), 18 events take place on the nightside of northern polar cusp, cap and/or lobes, with an event magnetic latitude of $\sim N30^\circ$ – $N45^\circ$; the other 10 events happen in the southern polar cusp, cap and/or lobes with an event magnetic latitude of $\sim S45^\circ$ – $S65^\circ$, including 6 on the dayside and 4 in the post-midnight sector. These DEE events may be the counterparts of >40 keV electrons detected occasionally by the Cluster spacecraft in the higher-altitude cusp (Zhang et al. 2005). In addition, the nightside DEEs tend to exhibit a stronger electron flux and roughly sharper energy spectrum than the dayside DEEs (Fig. 14).

Therefore, the observed DEE events in the polar cusp, cap and/or lobes likely come from the solar wind superhalo electrons entering the magnetosphere via reconnection at the magnetopause. Because the magnetic field strength in the polar cusp and cap is the local minimum, the entering superhalo electrons can be trapped in these regions due to magnetic mirror effects (Zong et al. 2004, 2005). These electrons could undergo some acceleration via magnetopause reconnection, or some local acceleration (e.g., by wave-particle interactions.) in the trapped regions. Such an acceleration process would be more efficient at low energies than at high energies, in order to produce a DEE energy spectrum sharper than the energy spectrum

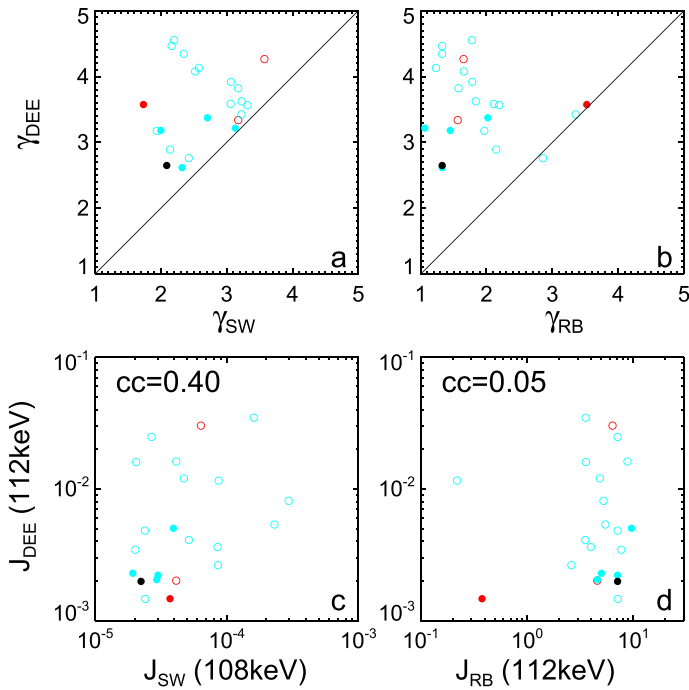


Fig. 14 Scatter plots of the DEEs versus solar wind superhalo electrons (left) and radiation belt electrons (right) for the 22 events with good observations of electron flux energy spectrum. Top: power-law spectral index. Bottom: electron differential flux at ~110 keV. The blue (red) symbols denote the DEE events with an average southward (northward) B_z of OMNI IMF, while the black symbols show the DEE events with no available OMNI data. The solid (open) symbols denote the DEE events occurring at the dayside (nightside) of polar magnetospheric regions

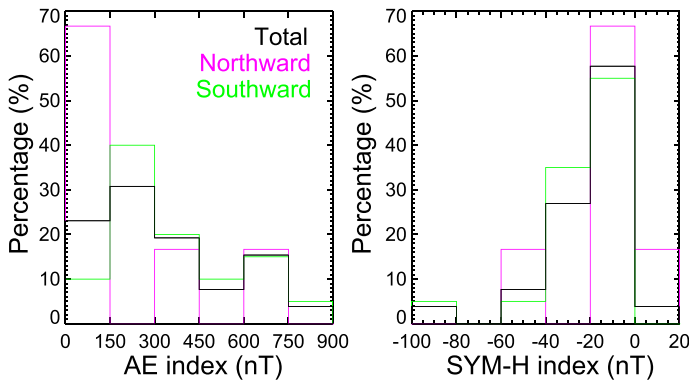


Fig. 15 Histograms of the average AE index (left) and average SYM-H index (right) for the 28 DEE events. The black histogram represents all the events, while the pink (green) histogram shows the events with an average northward (southward) B_z of OMNI IMF

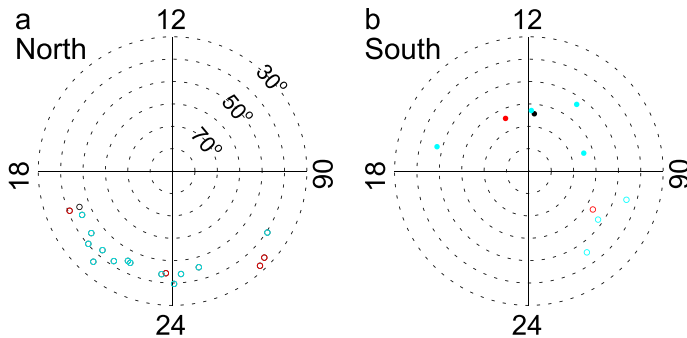


Fig. 16 The IGSO BeiDou satellite's location in the format of GSM latitude and longitude (MLT) for the 28 DEE events. The blue (red) symbols denote the DEE events with an average southward (northward) Bz of OMNI IMF, while the black symbols show the DEE events with no available OMNI data. The solid (open) symbols denote the DEE events occurring at the dayside (nightside) of polar magnetospheric regions

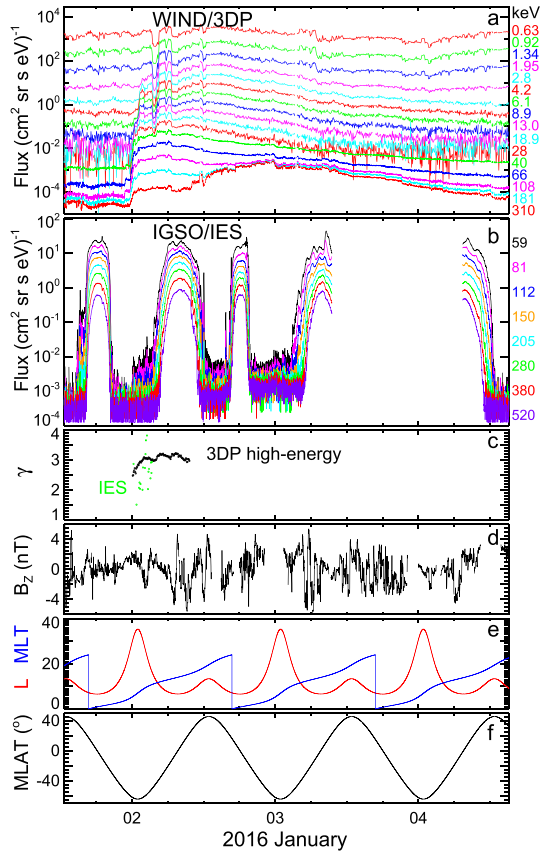
of source superhalo electrons, while it would also be more efficient on the nightside than on the dayside.

3.2 Solar energetic electron origin

After surveying the BD-IES and Wind/3DP electron observations from October 2015 through January 2016 (Wang et al. 2021), we discovered the observational evidences for the direct and continuous entry of SEEs from the IPM to the Earth's polar cusp, cap and/or lobes during three SEE events, respectively, in October 2015, November 2015 and January 2016. During these SEE events, the BD-IES observations in the high-altitude polar cusp, cap and/or lobes (when available) exhibit significant electron fluxes at energies of $\sim 50\text{--}200$ keV, when the >50 keV electron fluxes detected by Wind/3DP around the L1 point are high enough. In addition, such BD-IES fluxes show a fast-rise slow-decay temporal profile and a single-power-law energy spectrum, in agreement with the SEE measurements by Wind/3DP at similar energies in the IPM.

In the January 2016 SEE event (Fig. 17), the electron fluxes detected by Wind/3DP start to rapidly increase at 2335UT on January 1 with a clear energy dispersion at $\sim 1\text{--}310$ keV, rise to a gradual peak, and then decrease very slowly for over 2 days. Such temporal flux profiles are caused by the arrival of SEEs at the Wind spacecraft. During the event slow-decay phase, another flux enhancement begins near 0800UT on January 2 with an energy dispersion at $108\text{--}310$ keV, which is due to contaminations by the high-energy solar energetic protons accompanied with this SEE event. Furthermore, the background-subtracted electron flux energy spectrum detected by Wind/3DP mostly fit to a double-power-law function of Eq. (1) with a downward-bending break E_{br}^{3DP} near 60 keV (Fig. 19). At energies above E_{br}^{3DP} , the fitted power-law index γ_{3DP} increases over time from ~ 2.5 to ~ 3 and then stays more or less around 3 (Fig. 17), before the occurrence of solar energetic proton contaminations.

Fig. 17 Temporal profiles of the January 2016 SEE event. **a** Electron omnidirectional differential fluxes detected by WIND/3DP at 0.63–310 keV around the L1 point. **b** Electron omnidirectional differential fluxes measured by BD-IES at 59–520 keV in the IGSO orbit. **c** Electron spectral indexes measured by BD-IES (green) and by Wind/3DP at energies above the downward break (black). The shown spectral indexes are obtained by considering the uncertainties both in electron flux and energy (Liu et al. 2020). **d** The OMNI IMF Bz component in the GSM coordinates. **e** L shell (red) and MLT (blue) along the IGSO orbit. **f** Magnetic latitude along the IGSO orbit. Figure is taken from Wang et al. (2021)



During the January 2016 SEE event, the IGSO BeiDou satellite passes the polar cusp, cap, and/or lobes several times with the available BD-IES measurements (Figs. 17 and 18). During its southern cusp/cap/lobe passage from 2050UT on January 1 to 0325UT on January 2 (Figs. 17 and 18), the BD-IES measurements at energies of 59–205 keV begin to show significant electron fluxes (well over the instrumental noise) at ~0000UT on January 2, while those at higher energies are predominated by instrumental noise. During 0000UT–0325UT on January 2, the temporal flux profiles measured by BD-IES at 59–205 keV appear similar to the temporal flux profiles of SEEs observed simultaneously by Wind/3DP at 40–310 keV in the IPM (Fig. 19). After removal of instrumental noise, the 5-min average electron flux measured by BD-IES, J_{IES} , shows a strong correlation with the 5-minute average flux of SEEs detected by Wind/3DP, J_{3DP} , at the same/similar energy (Fig. 19). The average flux ratio of J_{IES}/J_{3DP} is ~0.6 at ~60 keV. In addition, J_{IES} can fit to a single-power-law energy spectrum at 59–205 keV, $J \propto E^{-\gamma}$, similar to the SEEs detected by Wind/3DP at similar energies. Therefore, these 59–205 keV electrons observed by BD-IES come from the entering SEEs from the IPM in the polar cusp, cap and/or lobes. The power-law index of

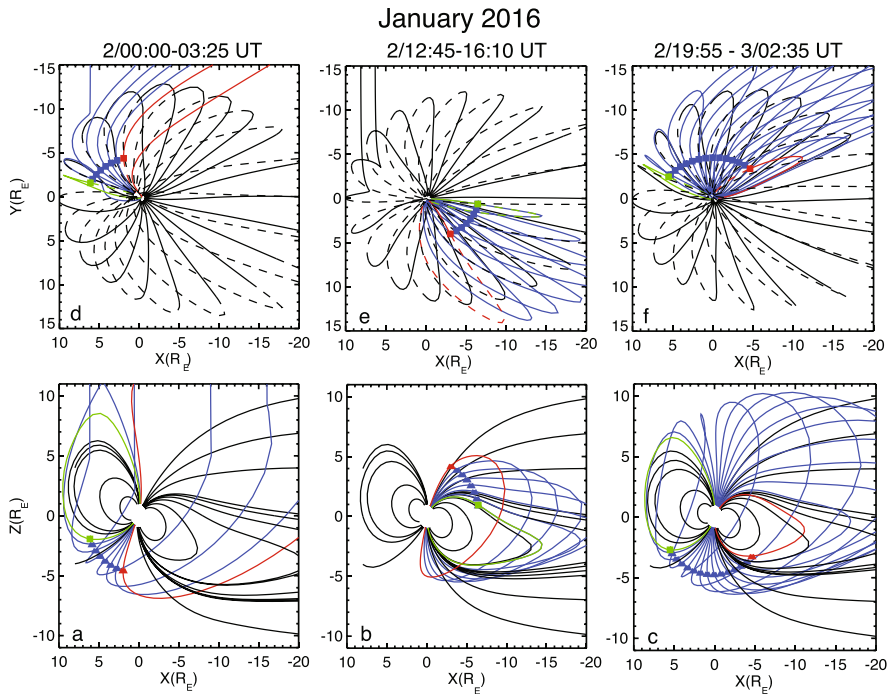


Fig. 18 Average configuration of magnetospheric magnetic field lines during the three polar passages of BeiDou satellite with the BD-IES observations of SEEs, estimated by the T96 model, for the January 2016 event. **a–c** Projection onto the GSE X – Y plane. **d–f** Projection onto the GSE X – Z plane. In each polar passage, this IGSO satellite (shown as solid symbols) is connected to the red (green) magnetic field line at the start time (end time) of BD-IES SEE observations. Figure is taken from Wang et al. (2021)

BD-IES electrons, γ_{IES} , significantly grows over time from ~ 1.5 to ~ 4 (Fig. 17), while it is not correlated to the Wind/3DP index γ_{3DP} (Fig. 19).

During the northern cusp/cap/lobe passage of the BeiDou satellite from 1245UT to 1610UT on January 2 (Figs. 17 and 18), the BD-IES observations at energies of 59–112 keV keep exhibiting significant electron fluxes, with a slow-decay profile similar to the temporal flux profile of SEEs measured simultaneously by Wind/3DP at similar energies; the BD-IES observations at higher energies begin to show a slow-rise profile, also close to the Wind/3DP temporal flux profile caused by solar energetic proton contaminations at similar energies. Thus, these BD-IES observations at 59–112 keV are also due to the entering SEEs from the IPM in the polar cusp, cap and/or lobes, while those at 150–520 keV are mostly contaminations caused by the entering solar energetic protons.

During the southern cusp/cap/lobe passage from 1955UT on January 2 to 0235UT on January 3, the BD-IES measurements are due to solar energetic proton contaminations. During the northern passage from 1255UT–1555UT on January 4, the BD-IES measurements become predominated by instrumental noise, since the simultaneous Wind/3DP fluxes of SEEs decrease to a rather low

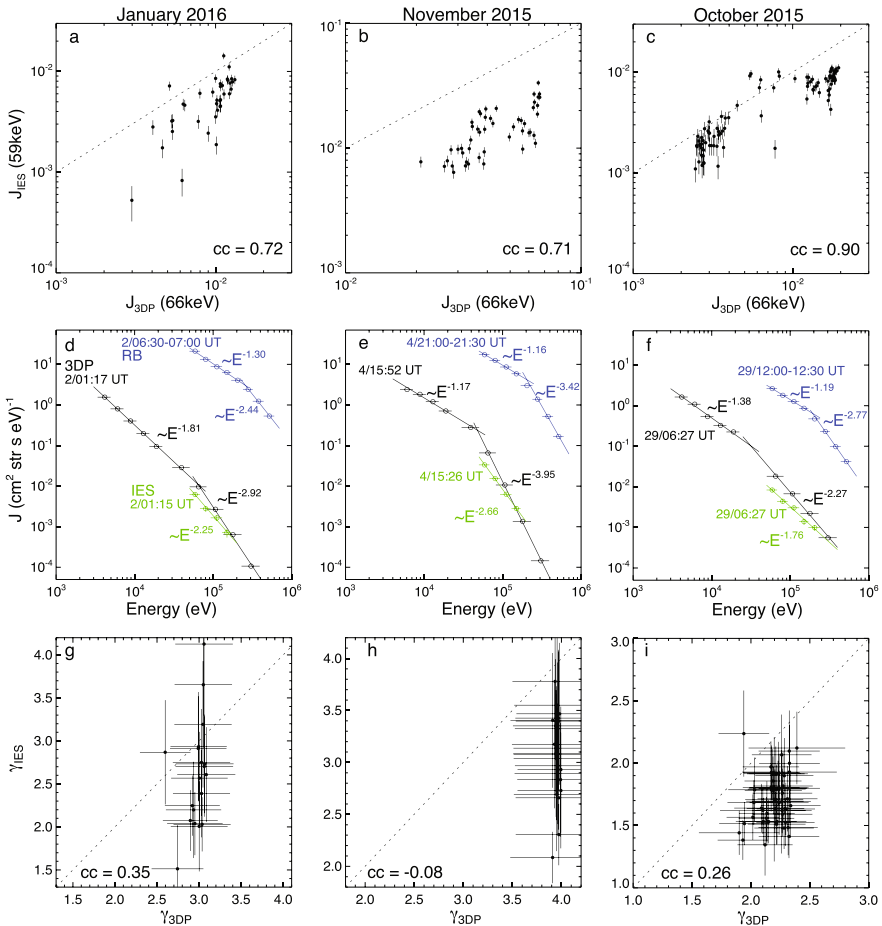
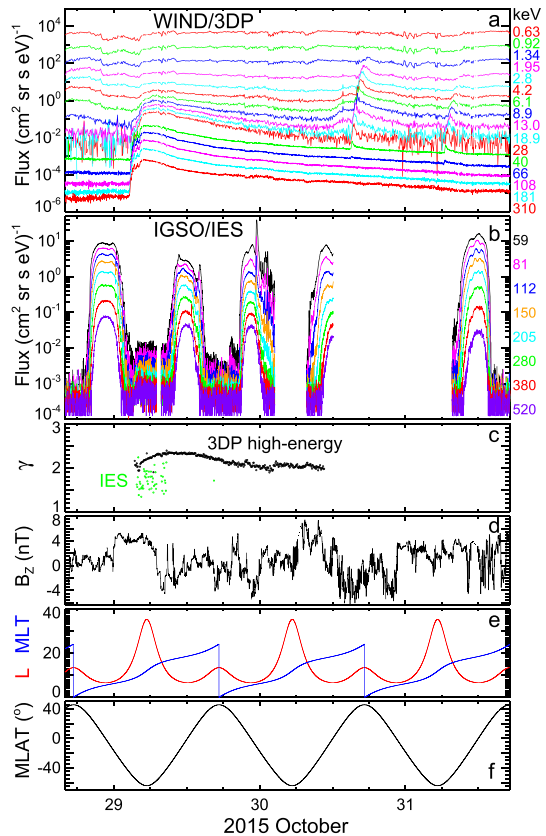


Fig. 19 Comparison between the Wind/3DP and BD-IES electron observations for the three SEE events. **a–c** Scatter plots between the Wind/3DP electron flux and BD-IES electron flux detected simultaneously at ~ 60 keV. **d–f** Flux energy spectra of SEEs detected by BD-IES (green) and by Wind/3DP (black) at similar/same times. The blue circles denote the representative energy spectrum of outer radiation belt electrons measured by BD-IES on the same day, which generally fits to a double-power-law function (Equation 1) with a downward-bending break near 150–200 keV (Wang et al. 2017). **g–i** Scatter plots between the Wind/3DP electron spectral index and BD-IES spectral index detected simultaneously at similar energies. Figure is taken from Wang et al. (2021)

intensity at the L1 point. Also note that the BD-IES instrument generally detects high-flux energetic electrons in outer radiation belts with a typical double-power-law flux energy spectrum bending downwards at a spectral break near 140 keV, during the low-latitude trajectories of BeiDou satellite between every two cusp/cap/lobe passages (Wang et al. 2017, 2021; Zong 2018).

During the other two SEE events, respectively, in October and November 2015 (Figs. 20 and 21), the BD-IES observations in the high-altitude polar cusp, cap and/or lobes also appear to exhibit significant electron fluxes (the

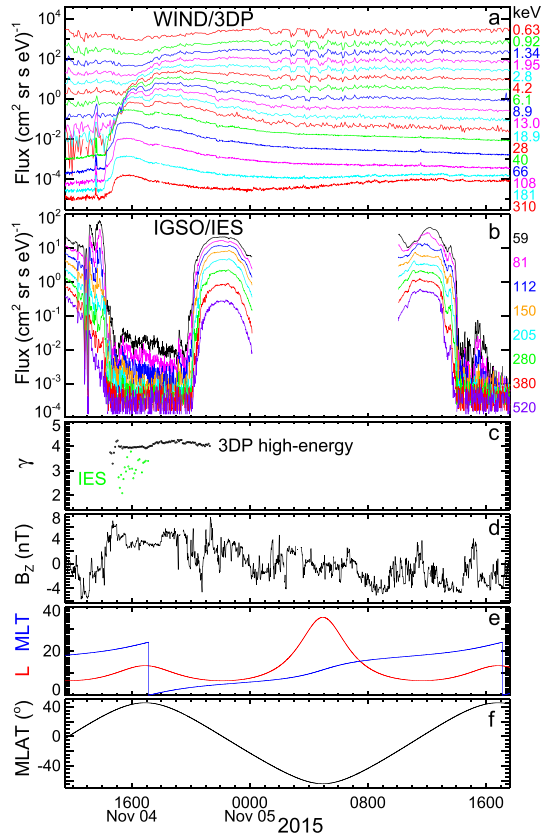
Fig. 20 Temporal profiles of the October 2015 SEE event. **a** Electron omnidirectional differential fluxes detected by WIND/3DP at 0.63–310 keV around the L1 point. **b** Electron omnidirectional differential fluxes measured by BD-IES at 59–520 keV in the IGSO orbit. **c** Electron spectral indexes measured by BD-IES (green) and by Wind/3DP at energies above the downward-bending break (black). **d** The OMNI IMF B_z component. **e** L shell (red) and MLT (blue) along the IGSO orbit. **f** Magnetic latitude along the IGSO orbit. Figure is taken from Wang et al. (2021)



instrumental noise), when the SEE fluxes detected by Wind/3DP around the L1 point are high (low) at similar energies. In addition, these BD-IES electrons show a fast-rise slow-decay flux temporal profile and a single-power-law flux energy spectrum, which is consistent with the interplanetary SEEs detected by Wind/3DP but different from the outer radiation belt electrons detected by BD-IES at similar energies. On the other hand, some spike-like electron events take place during the temporal decay phase detected by BD-IES, e.g., a 59–205 keV spike during 1900UT–2035UT on October 29 and a 59–150 keV spike during 1905UT–1930UT on November 4. These spike-like electron events could come from the entering SEEs that undergo some further local acceleration in the polar cusp, cap and/or lobes, analogous to the DEE events.

In all the three SEE events, the background-subtracted electron differential fluxes detected by BD-IES in the polar cusp, cap and/or lobes are strongly correlated with the SEE differential fluxes measured concurrently at comparable energies by Wind/3DP around the L1 point (Fig. 19). According to a cross correlation analysis of two time series $J_{\text{IES}}(t)$ and $J_{\text{3DP}}(t - \Delta t)$ (Fig. 22), the possible time lag (Δt) of the BD-IES fluxes after the Wind/3DP fluxes is ~ 0 –10 minutes for the

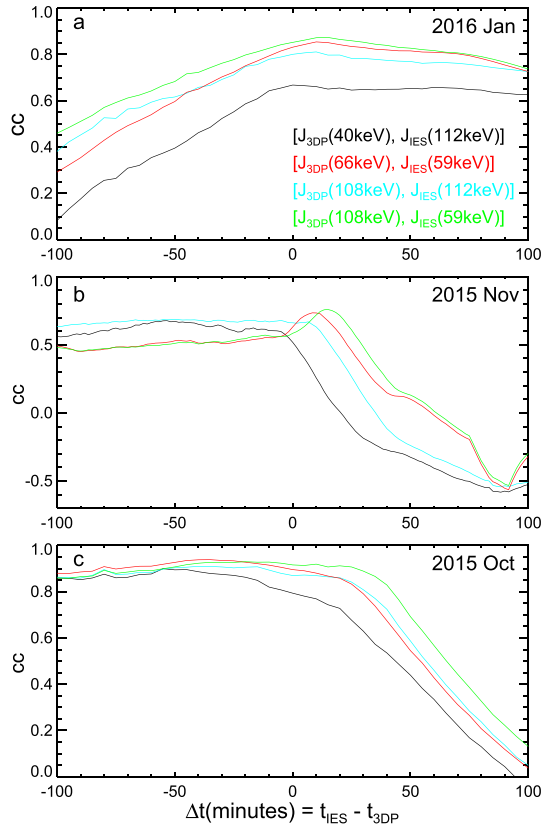
Fig. 21 Temporal profiles of the November 2015 SEE event. **a** Electron omnidirectional differential fluxes detected by WIND/3DP at 0.63–310 keV around the L1 point. **b** Electron omnidirectional differential fluxes measured by BD-IES at 59–520 keV in the IGSO orbit. **c** Electron spectral indexes measured by BD-IES (green) and by Wind/3DP at energies above the downward-bending break (black). **d** The OMNI IMF Bz component. **e** L shell (red) and MLT (blue) along the IGSO orbit. **f** Magnetic latitude along the IGSO orbit. Figure is taken from Wang et al. (2021)



November 2015 event and January 2016 event, and is ~ -30 – 10 min for the October 2015 event. Furthermore, the electron characteristics (such as the flux intensity, flux temporal profile and flux energy spectrum) detected by BD-IES in high-altitude polar cusp, cap and/or lobes are unaffected by the occurrence of either a southward or northward component of IMF at the bow shock's nose (Figs. 17, 20 and 21). These evidences show that the SEEs can directly and continuously enter from the IPM into the planet's polar magnetospheric regions and then become trapped over there.

Furthermore, the SEE fluxes observed by BD-IES in high-altitude polar cusp, cap and/or lobes are mainly lower than the SEE fluxes measured simultaneously by Wind/3DP around the L1 point, specifically at lower energies. Therefore, the SEE flux energy spectrum in these polar magnetospheric regions is mostly flatter (harder) than the simultaneous SEE spectrum in the IPM. It indicates that the SEE entry/trapping into the magnetosphere could be less effectively at low energies than at high energies. The fitted power-law spectral index of SEEs detected by BD-IES also tends to increase significantly over time, but it is not correlated with the SEE spectral index measured simultaneously by Wind/3DP.

Fig. 22 Cross correlation analysis between the two time series of the 1 minute-average $J_{IES}(t)$ and 1 minute-average $J_{3DP}(t - \Delta t)$ for the three SEE events. The red, blue, black and green curves show the cross-correlation coefficients, respectively, between J_{3DP} at 66 keV and J_{IES} at 59 keV, between J_{3DP} at 108 keV and J_{IES} at 112 keV, between J_{3DP} at 40 keV and J_{IES} at 112 keV, and between J_{3DP} at 108 keV and J_{IES} at 59 keV



4 Summaries

Interplanetary energetic electrons, consisting of continuous solar wind superhalo electrons and occasional transient SEE events, can provide a source of energetic electrons for the Earth's magnetosphere. Using the energetic electron measurements from BD-IES onboard one IGSO Beidou navigation satellite in the high-altitude polar cusp, cap and/lobes, we found the first evidences for the direct and continuous entry of energetic electrons from the IPM to Earth's magnetosphere (Wang et al. 2017, 2021), regardless of a southward or northward component of IMF.

When interplanetary energetic electrons are made up of continuous superhalo electrons in solar wind, the BD-IES measurements in high-altitude polar cusp, cap and/lobes are mostly predominated by instrumental noise, since the superhalo electron fluxes are generally low; sometimes, however, the BD-IES measurements in these polar magnetospheric regions exhibit some occasional spike-like DEE events. Compared to the superhalo electrons measured simultaneously in the IPM, these DEE events show a roughly correlated flux but with the ~ 10 – 1000 times enhanced intensity, while they also exhibit a single-power-law flux energy spectrum but typically with a steeper (softer) slope. These DEE events are probably formed by

some local acceleration or magnetopause reconnection acceleration on the entering superhalo electrons from the IPM into the polar magnetospheric regions.

When interplanetary energetic electrons are predominated by SEEs with high (low) fluxes, the BD-IES observations in high-altitude polar cusp, cap and/lobes exhibit significant fluxes of the SEEs entering in these regions (the instrumental noise) at similar energies. Compared to the SEEs observed in the IPM, these entering SEEs exhibit a similar temporal flux profile with a lower intensity and a possible time lag within ~ 10 min; these entering SEEs also have a similar flux energy spectrum but mostly with a flatter (harder) slope. Thus, the entry/trapping of SEEs in the magnetosphere could be more effectively at higher energies. In addition, the SEE fluxes measured in polar magnetospheric regions are occasionally superimposed by some spike-like events that are probably produced by some local acceleration or magnetopause reconnection acceleration on these entering SEEs.

These studies indicate that interplanetary energetic electrons can make a possible contribution to the formation of energetic electrons in the planetary's magnetosphere. However, these studies sampled only a limited number of DEE events and SEE events, and lacked the magnetic field measurements to examine the characteristics of electron pitch angle distributions in the terrestrial polar cusp/cap/lobe regions. Future studies would systematically and statistically compare the energetic electron observations among the IPM, polar magnetospheric regions, and radiation belts, as well as combining with the in situ plasma and magnetic field observations, to further investigate the interplanetary contribution to magnetospheric energetic electrons.

Acknowledgements I would like to thank Professor Qiugang Zong for helpful discussions. I also acknowledge the BD-IES team and Wind/3DP team for providing the electron measurements, and NASA CDAWeb data service for the GOES and OMNI data. This work is supported in part by NSFC under contracts 42127803 and 42150105, and by the China National Space Administration Project (D020301).

Declarations

Conflict of interest The author states that there is no conflict of interest.

Open Access This article is licensed under a Creative Commons Attribution 4.0 International License, which permits use, sharing, adaptation, distribution and reproduction in any medium or format, as long as you give appropriate credit to the original author(s) and the source, provide a link to the Creative Commons licence, and indicate if changes were made. The images or other third party material in this article are included in the article's Creative Commons licence, unless indicated otherwise in a credit line to the material. If material is not included in the article's Creative Commons licence and your intended use is not permitted by statutory regulation or exceeds the permitted use, you will need to obtain permission directly from the copyright holder. To view a copy of this licence, visit <http://creativecommons.org/licenses/by/4.0/>.

References

- T. Asikainen, K. Mursula, *Ann. Geophys.* **24**, 1949–1956 (2006)
- J.L. Burch, T.E. Moore, R.B. Torbert, B.L. Giles, *Space Sci. Rev.* **199**, 5 (2016). <https://doi.org/10.1007/s11214-015-0164-9>
- C.M. Cohen, G. Li, G.M. Mason, A.Y. Shih, L. Wang, Solar energetic particles. In *Book: Solar Physics and Solar Wind*, edited by Nour E. Raouafi, Angelos Vourlidis, Yongliang Zhang, Larry J. Paxton,

- Geophysical Monograph Series, page 133–178 (2021) <https://agupubs.onlinelibrary.wiley.com/doi/10.1002/9781119815600.ch4>
- N. Dresing, F. Effenberger, R. Gómez-Herrero, B. Heber, A. Klassen, A. Kolhoff, I. Richardson, S. Theesen, *Astrophys. J.* **118**, 49 (2020)
- C.P. Escoubet, M. Fehringer, M. Goldstein, *Ann. Geophys.* **19**, 1197–1200 (2001). <https://doi.org/10.5194/angeo-19-1197-2001>
- L.A. Fisk, G. Gloeckler, N.A. Schwadron, *Astrophys. J.* **720**, 533 (2010)
- N.J. Fox, M.C. Velli, S.D. Bale et al., *Space Sci. Rev.* **204**, 7 (2016)
- G.J. Hurford et al., *Astrophys. J.* **192**, 541 (1974)
- S. Krucker, P.H. Oakley, R.P. Lin, *Astrophys. J.* **691**, 806 (2009)
- R.P. Lin, *Space Science Reviews* **16**, 189 (1974)
- R.P. Lin, *Sol. Phys.* **100**, 537 (1985)
- R.P. Lin, *A.I.P. Conf. Proc.* **385**, 25 (1997)
- R.P. Lin et al., *Space Sci. Rev.* **136**, 241 (2008)
- R.P. Lin, K.A. Anderson, S. Ashford et al., *Space Sci. Rev.* **71**, 125 (1995)
- Z. Liu, L. Wang, Q. Shi, M. Oka, L. Yang, R.F. Wimmer-Schweingruber et al., *Astrophys. J.* **889**, L2 (2000)
- Z. Liu, L. Wang, R. F. Wimmer-Schweingruber, S. Krucker, G. M. Mason, *J. Geophys. Res.*, 125, e2020JA028702, (2020) <https://doi.org/10.1029/2020JA028702>
- J.G. Luhmann et al., *Space Sci. Rev.* **136**, 117 (2008)
- M. Maksimovic, V. Pierrard, P. Riley, *Geophys. Res. Lett.* **24**, 1151 (1997)
- G.M. Mason et al., *Space Sci. Rev.* **86**, 409 (1998)
- M.D. Montgomery, S.J. Bame, A.J. Hundhausen, *J. Geophys. Res.* **73**, 4999 (1968)
- D. Müller, O.C. Cyr, I. Zouganelis, H.E. Gilbert, R. Marsden, *Astron. Astrophys.* **642** (2020). <https://doi.org/10.1051/0004-6361/202038467>
- K. Nykyri, A. Otto, E. Adamson, E. Kronberg, P. Daly, *J. Atmos. Solar-Terrest. Phys.* **87**, 70 (2012). <https://doi.org/10.1016/j.jastp.2011.08.012>
- K. Nykyri, C. Chu, X. Ma, S.A. Fuselier, R. Rice, *J. Geophys. Res.* **124**, 197 (2019). <https://doi.org/10.1029/2018JA026131>
- E.N. Parker, *Astrophys. J.* **330**, 474 (1988)
- W.G. Piliipp et al., *J. Geophys. Res.* **92**, 1075 (1987)
- H. Rosenbauer, R. Schwenn, E. Marsch et al., *J. Geophys. Res.* **42**, 561 (1977)
- J.D. Scudder, *Astrophys. J.* **398**, 299 (1992)
- R.B. Sheldon, H.E. Spence, J.D. Sullivan et al., *Geophys. Res. Letts.* **25**, 1825–1828 (1998)
- Š. Štverák, M. Maksimovic, P.M. Trávníček, et al. *J. Geophys. Res.*, 114 (2009)
- J. Tao, L. Wang, G. Li et al., *Astrophys. J.* **922**, 198 (2021)
- B.M. Walsh, T.A. Fritz, M.M. Klida, J. Chen, *Ann. Geophys.* **28**, 983–992 (2010)
- L. Wang, PhD thesis, Univ. California, Berkeley, Publication Number: AAT 3402669 (2009)
- L. Wang, R.P. Lin, S. Krucker, J.T. Gosling, *Geophys. Res. Lett.* **33**, L03106 (2006). <https://doi.org/10.1029/2005GL024434>
- L. Wang, R.P. Lin, C. Salem et al., *Astrophys. J. Lett.* **753**, L23 (2012a)
- L. Wang, R.P. Lin, S. Krucker, G.M. Mason, *Astrophys. J.* **759**, 69 (2012b)
- L. Wang, L. Yang, J. He et al., *Astrophys. J. Lett.* **803**, L2 (2015)
- L. Wang, Q. Zong, Q. Shi et al., *Sci. China Tech. Sci.* **60**, 1935–1940 (2017). <https://doi.org/10.1007/s11431-017-9119-x>
- L. Wang, Q. Zong, Q. Shi et al., *Astrophys. J.* **910**, 12 (2021)
- L. Yang, L. Wang, G. Li et al., *Astrophys. J. Lett.* **811**, L8 (2015). <https://doi.org/10.1088/2041-8205/811/1/L8>
- L. Yang, L. Wang, J. He et al., *RAA* **15**, 348 (2015). <https://doi.org/10.1088/1674-4527/15/3/005>
- L. Yang, L. Wang, G. Li et al., *Astrophys. J.* **875**, 104 (2019)
- P.H. Yoon et al., *Astrophys. J.* **868**, 131 (2018)
- P.H. Yoon, L.F. Ziebell, R. Gaelzer, R.P. Lin, L. Wang, *Space Sci. Rev.* (2012). <https://doi.org/10.1007/s11214-012-9867-3>
- G.P. Zank, J.A. Roux, G.M. Webb et al., *Astrophys. J.* **797**, 28 (2014)
- H. Zhang, T.A. Fritz, Q.G. Zong et al., *J. Geophys. Res.* **110**, A05211 (2005)
- Q. Zong et al., *Space Weather* **16**, 121–125 (2018)
- Q.G. Zong, T.A. Fritz, H. Zhang et al., Triple cusps observed by cluster-temporal or spatial effect? *Geophys. Res. Lett.* **31**, L09810 (2004)

- Q. Zong, T.A. Fritz, H.E. Korth et al., *Surv. Geophys.* **26**, 215–240 (2005). <https://doi.org/10.1007/s10712-005-1879-z>
- Zong, Q., Hao, Y., Zou, H., et al. *Sci. China Tec. Sci.*, 59, 1-9 (2016)
- Q. Zong, Y. Cao, S. Fu, *Space Sci. Rev.* **217**, 1–34 (2021)

Publisher's Note Springer Nature remains neutral with regard to jurisdictional claims in published maps and institutional affiliations.